Supporting Information

Light-Induced Beneficial Ion Accumulation for High-Performance Quasi-2D Perovskite Solar Cells

Xiaomei Lian,[a]‡ Lijian Zuo,[a,b*]‡ Bowen Chen,[d]‡ Biao Li,[c]‡ Haotian Wu,[a] Shiqi Shan,[a] Gang Wu,[a] Xuegong Yu,[c*] Qi Chen,[d*] Liwei Chen,[d] Deren Yang,[b,c] David Cahen,[e*] Hongzheng Chen[a*]

[a.] *State Key Laboratory of Silicon Materials, MOE Key Laboratory of Macromolecular Synthesis and Functionalization, Department of Polymer Science and Engineering, Zhejiang University, Hangzhou 310027, P. R. China.Address here. E-mail: zjuzlj@zju.edu.cn; hzchen@zju.edu.cn*

[b.] *Zhejiang University-Hangzhou Global Scientific and Technological Innovation Center, Hangzhou 310014, P. R. China.*

[c.] *State Key Laboratory of Silicon Materials, School of Materials Science and Engineering, Zhejiang University, Hangzhou 310027, P. R. China. E-mail: yuxuegong@zju.edu.cn*

[d.] *i-Lab, CAS Center for Excellence in Nanoscience, Suzhou Institute of Nano-Tech and Nano-Bionics, Chinese Academy of Sciences, Suzhou 215123, P. R. China. E-mail: qchen2011@sinano.ac.cn*

[e.] *Bar Ilan Institute for Nanotechnology & Advanced Materials, BINA & Chemistry Department, Bar Ilan University, Ramat Gan, 5290002, and Dept. of Mol. Chem. and Mater. Sci., Weizmann Inst. of Science, Rehovot, 7610001, Israel. E-mail: david.cahen@weizmann.ac.il*

Keywords: perovskite solar cells, quasi-2D perovskite, ion accumulation, light activation, build-in potential

Materials and Methods

Materials

Butylamine hydroiodide (BAI, 99%), guanidinium chloride (GACl, 99%), (6,6)-Phenyl-C_{61}-butyric acid methyl ester (PCBM, 99%), poly[bis(4-phenyl)(2,4,6-trimethylphenyl) amine](PTAA, 99%), and PbI_2 (99%) were purchased from Xi'an Polymer. Bathocuproine (BCP, 99%) was purchased from TCI. Methylammonium iodide (MAI, 99%) was purchased from Shanghai Mater Win New Materials. N, N-dimethylformamide (DMF, 99%) was purchased from Alfa Aesar. Formamide (99.5%), chloroform (CF, 99%), and ethyl alcohol (99%) were obtained from Sigma Aldrich. Poly [(9,9-bis(3'-(N, N-dimethyl)-nethylammonium-propyl)-2,7-fluorene)-alt-2,7-(9,9–dioctylfluorene)]dibromide (PFN-Br, 99%) was purchased from Solarmer Materials Inc. All the reagents and solvents were used directly unless specified otherwise.

Device Fabrication and Characterization

ITO-coated glass substrates were cleaned sequentially in detergent (Hellmanex III, 2 vol%), deionized water, acetone, and isopropanol in an ultrasonic bath for 15 min, respectively. Thereafter, the substrates were dried under nitrogen flow and cleaned using UV-ozone treatment for 20 min before use. We prepared PTAA hole transport layer (HTL) (from 2 mg/ml in toluene) by spin-coating at 4000 rpm for 40 s, and then spin-coated PFN-Br (0.5 mg/ml in methanol) atop of PTAA, followed by annealing at 100 °C for 10 min. BAI, GACl, MAI, and PbI_2 were mixed at a molar ratio of 1.8:0.2:5:6 in DMF at a concentration of 0.6M (based on PbI_2). The perovskite precursor solution and PTAA substrates were heated to 70 °C and 100 °C, respectively, before the spin-coating of the perovskite layer. The spin-coating process was initiated at 4000 rpm for 30 s after dropping the hot perovskite precursor to the preheated PTAA substrate, with 150 ml of toluene added to the perovskite at 10 s, and then PCBM was spin-coated on the perovskite film at 2000 rpm for 30 s, followed by annealing at 100 °C for 10 min. BCP was then spin-coated on PCBM at 4000 rpm for 30 s, followed by depositing 100 nm of Ag in a vacuum chamber at a high vacuum pressure of 3×10^{-4} Pa. The devices were then treated under different thermal-annealing temperatures and light intensities for different times. The heat-light co-treated devices were prepared at 100 ^{o}C (or other temperatures), with the white light in the laboratory and glovebox turn on. The devices thermal-treated in dark were prepared by annealing the devices at 100 ^{o}C with a lid of petri dish, and the petri dish was wrapped with foil to isolate the light.

For the perovskite crystal, both the cation (MA^+) and anion (I^-) are easily to migrate. The ion migration will cause interstitial defects at the interfaces and vacancy defects in the bulk. Under the electrical bias, the I^- and MA^+ ions tend to migrated toward opposite direction, and then accumulated at cathode and anode interface, respectively, with MA^+ ion the same direction as the electric field. This process is accelerated by thermal annealing. The ion migration rate is highly temperature dependent, following the Arrhenius relationships:

$$\ln(k)=-E_a/RT+\ln(A)$$

Both Mott-Schottky characterization and TID measurements was performed on Fourier Transform, High Energy Resolution Analysis and Deep Level Transient Spectroscopy (FT 1030 HERA-DLTS).

Mott-Schottky characterization

Mott-Schottky characterization was performed to obtain the needed data for TID method in equation S1. The junction capacitance of PVSCs is described by equation S1. The dopant concentrations (N_d) and built-in potential (V_{bi}) were deduced by linear fitting of the C^{-2}-V curve. Here, relative dielectric constant of 24 was used for both 2D and 3D PVSCs. The figure below shows the Mott-Schottky characterization, i.e., (1/C2)-V plots for the quasi-2D PVSC (a) and 3D PVSC (b). It is illustrated that the built-in potential for 2D and 3D PVSCs are 1.36 V and 1.26 V, respectively. In addition, the concentration of dopants for 2D and 3D PVSCs are 5.00×10^{15} cm^{-3} and 3.69×10^{15} cm^{-3}.

$$C = A\sqrt{\frac{q\varepsilon\varepsilon_0 N_d}{2(V_{bi}-V)}} \quad \text{(S1)}$$

C is the capacitance. A is the area of the device. ε_0 is vacuum dielectric constant. ε is the relative dielectric constant for the light absorbing layer. q is elemental charge. N_d is the dopants concentration. V is the applied bias. V_{bi} is the built-in potential.

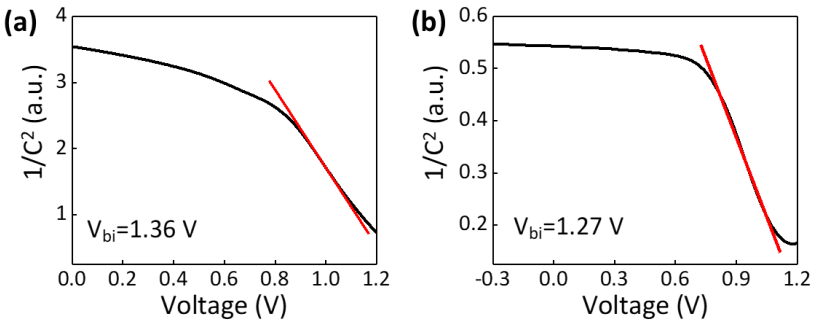

Transient ion-drift (TID) measurements

The TID method is first applied into PVSCs and is well studied by Futscher et al.[1] TID method is able to extract multiple ion migration parameters, including the activation energy, ion diffusion coefficient and the concentration of mobile ions. A characteristic advantage of TID method is that it can distinguish anions from cations. This unique advantage is originated from the fact that moving ions with different type of charge induce different capacitance transient as presented in equation S2. Equation S2 is the modified version of equation S1. The existence of ions contributes to the concentration of space charge in the absorber layer. Here, the concentration of space charge is modified as $N_d \pm N_{ion}$. We refer $N_d \pm N_{ion}$ as the net concentration of space charge in the absorber layer. If the moving ions has the same charge type as the minority carrier, the net concentration of space charge increases leading to an increased capacitance. Otherwise, opposite charged ions will result in a decreased capacitance. Therefore, different capacitance transient is strong evidence that ions with different charge types migrate in the absorber layer. For 2D PVSC, there is only one capacitance transient from 180 K to 300 K where the delta C decreases with time. According to equation S2, this result indicates ions with only one charge type migrate in the absorber layer. However, for 3D PVSC, the delta C increases with time at low temperature while decreases with time at high temperature. This result is strong evidence that both anions and cations migrate in the absorber layer. Since I^- is reported to have a lower activation energy than that of MA^+. Thus, the moving ion at low temperature is attributed to I^- and the moving ion at high temperature is attributed to MA^+.

$$C = A\sqrt{\frac{\varepsilon_0\varepsilon q(N_d \pm N_{ion})}{2(V_{bi}-V)}} \quad \text{(S2)}$$

N_{ion} is the concentration of the mobile ions.

TID method depends on the measurement of the capacitance transient of the sample. Herein, at a specific temperature, the capacitance transient was recorded at a forward bias of 0.8 V within a time duration of 2 s for both 2D and 3D PVSCs devices. Please note that ions are accumulated at the interface between the absorber and transporting layers driven by built-in potential before the forward bias is on. The application of forward bias allows the accumulated ions to migrate back to bulk of the absorber layer which will induce capacitance transient. Immediately after the forward bias, a bias of 0 V was added to the device for 2 s to recover the status of ion accumulation under

built-in potential. Then, the same procedure was repeated to obtain the capacitance at different temperatures from 180 K to 300 K.

The theory of deduction of the ion migration parameters is given as follows. First, the ion induced capacitance transient is changing with time as equation S3. τ is the time constant of the capacitance transient as presented in equation S4. N_d is the doping density of absorber layer which is derived by Mott-Schottky characterization. It is clearly demonstrated that D is the only unknown parameters in equation S4 since τ can be obtained by exponential fitting of the measured capacitance transient. In addition, diffusion constant D is related to activation energy through diffusion equation (S5). In consequent, Arrhenius equation (S6) is derived from equation S4 and equation S5. Equation S6 has the same form as the Arrhenius equation in the main text. In addition, the activation energy is derived according to the slope of the Arrhenius curve while intercept at longitudinal axis gives the exponential pre-factor of the diffusion equation. Hence, the activation energy and the diffusion coefficient at every temperature are derived. Eventually, the concentration of mobile ions can be estimated by equation S7 which is derived by Lyubomirsky et al.

$$\Delta C(t) = \Delta C_\infty \exp\left(-\frac{t}{\tau}\right) \tag{S3}$$

$$\tau = \frac{\varepsilon_0 \varepsilon k_B T}{q^2 D N_d} \tag{S4}$$

$$D = D_0 \exp\left(-\frac{E_A}{k_B T}\right) \tag{S5}$$

$$\ln\left(\frac{T}{\tau}\right) = \ln\left(\frac{q^2 N_d D_0}{\varepsilon_0 \varepsilon k_B}\right) - \frac{E_A}{k_B T} \tag{S6}$$

$$N_m \cong 2N_d \left(\frac{\Delta C_\infty}{C_R}\right) \tag{S7}$$

where ΔC_∞ equals $C(0) - C_R$. t is time. τ is time constant. k_B is Boltzmann constant, T is temperature (in K), D is the diffusion coefficient, D_0 is the exponential pre-factor and N_m is the concentration of mobile ions.

Scanning Kelvin probe microscopy (SKPM)

An Ilion+ 693 System (Gatan Inc.) was used to prepare the device cross-sections. The device was first mechanically cracked, and loaded into the vacuum sample chamber. Then, the device was cooled by liquid nitrogen and polished with an argon ion beam with a voltage of 5 keV for 3 hours.

The surface potential of the device cross-section was measured by the heterodyne frequency-modulation (FM) SKPM which was operated with a Cypher S AFM (Asylum Research, Oxford Instruments) and a HF2LI Lock-in Amplifier (Zurich Instruments) together in Ar-filled glove box. Cr/Au-coated conductive probe (NSC14, Mikromasch, Tallinn, Estonia) with a resonance frequency ω_0 of ~135 kHz and a spring constant of ~4 $N \cdot m^{-1}$ were employed to do the SKPM measurement. For the heterodyne FM-SKPM, the topography was imaged by standard AC mode; meanwhile, an additional AC voltage (3V in amplitude and ~760kHz in frequency ω_e) was applied to generate a sideband signal whose frequency ($\omega_0 + \omega_e$) was exactly the second-order resonance frequency of

the probe to obtain a good signal-to-noise ratio. Then, the DC voltage provided by the Lock-in Amplifier to nullify sideband signal was collected as surface potential. The device cross-section in the dark condition was used to measure the contact potential difference between the tip and the sample, which reflect the electrical potential distribution in the PSCs, from which the work function contrast between different layer can be attained.[2, 3]

The SKPM signal corresponds to the contact potential difference (CPD) profile between tip and the cross-section surface of the solar cells with (few 10 s of) nm-scale spatial resolution. The CPD reflects the electrochemical potential along the perovskite solar cell architecture. The gradient in electrochemical potential of bulk perovskite gives rise to significant band bending.[4, 5] The band bending for cathode of the devices with "N" is calculated by: +0.51 – (+0.18) = +0.33 eV, for the bulk perovskite is: +0.18 – (+0.33) = –0.15 eV, for anode is : +0.33 – (+0.19) = +0.14 eV, and V_{bi} = +0.33 – 0.15 + 0.14 = +0.32 eV. That is also the same for devices with "O" and "P". For device with "O", the band bending for cathode is: –0.16 – (–0.69) = +0.53 eV, for the bulk perovskite: –0.69 – (–0.69) = 0 eV, for anode is: –0.69 – (–1.04) = +0.35 eV, and V_{bi} = +0.53 + (+0.35) = +0.88 eV. For device with "P", the band bending for cathode is: +0.36 – (–0.24) = +0.60 eV, for the bulk perovskite is: –0.24 – (–0.59) = +0.35 eV, for anode is: –0.59 – (–0.93) = +0.34 eV, and V_{bi} = +0.60 + (+0.36) + (+0.34) = +1.29 eV. Therefore, compared to the device with "O", the V_{bi} of device with "N" decreased by: +0.88 – (+0.32) = +0.56 eV, and V_{bi} of device with "P" increased by: +1.29 – (+0.88) = +0.41 eV.

Transient photocurrent (TPC) measurements

For the TPC measurements, the device was held at a short circuit under steady-state conditions controlled by a small pulsed perturbation of excess charge carriers produced by an laser beam (470 nm). The TPC measurements were taken using the same setup as that for the TPV measurements but without the continuous white light, which was under a short circuit. The device was connected to an oscilloscope (50 Ω input impedance). The lifetime (τ) was calculated by fitting a single exponential function to the TPC decay curves.

Electrical poling

First, the device is wired with a copper clip, which is further connected to a adjustable stabilized DC power source (keithley 2400). The devices are further put on a hotplate with temperature of 100 ^{o}C and kept at dark. Different bias voltages, i.e., generated by the power source are applied during the heating for 3 h. Then the devices are moved out of the plate and cooled to room temperature before the bias voltage is stopped.

Supporting Figures

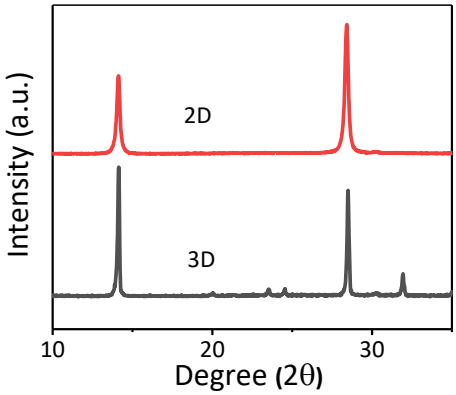

Figure S1. XRD patterns for 3D $MAPbI_3$ perovskite and quasi-2D $GA_{0.2}BA_{1.8}MA_5Pb_6I_{19}$ perovskite.

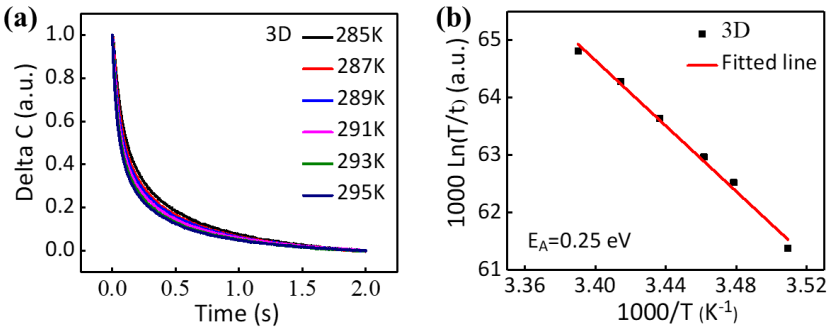

Figure S2. TID measurements for 3D PVCS: (a) capacitance transients for 285 K to 295 K. (b) Arrhenius fitting results from 285 K to 295 K.

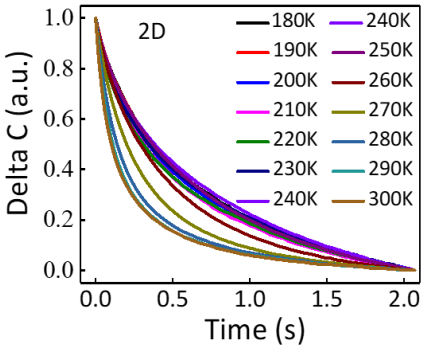

Figure S3. TID measurements for quasi-2D PVSCs from 180 K to 300 K.

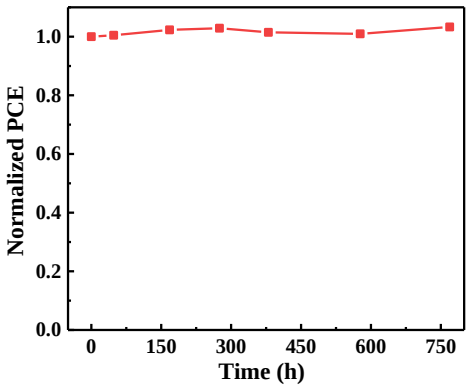

Figure S4. Variation in the PCE for quasi-2D based device in N_2 at room temperature in the dark.

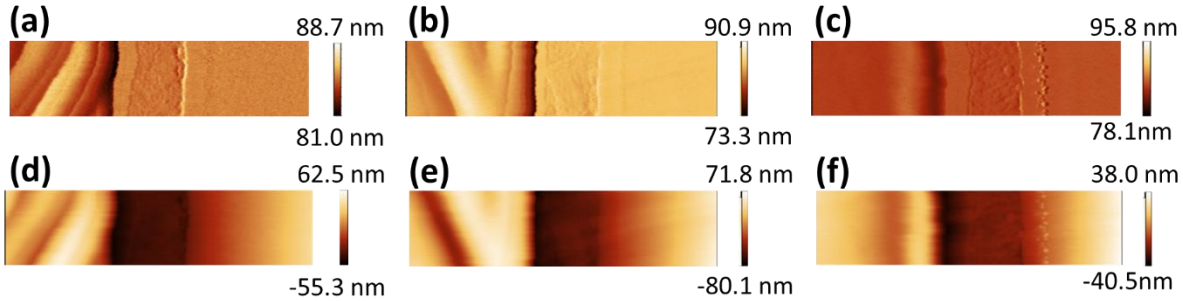

Figure S5. Topographic images taken on the cross-sectional surface for the quasi-2D $GA_{0.2}BA_{1.8}MA_5Pb_6I_{19}$ PVSC with (a, d) "O" (no ion accumulation), (b, e) "N" (unfavorable ion accumulation) and (c, f) "P" (favorable ion accumulation).

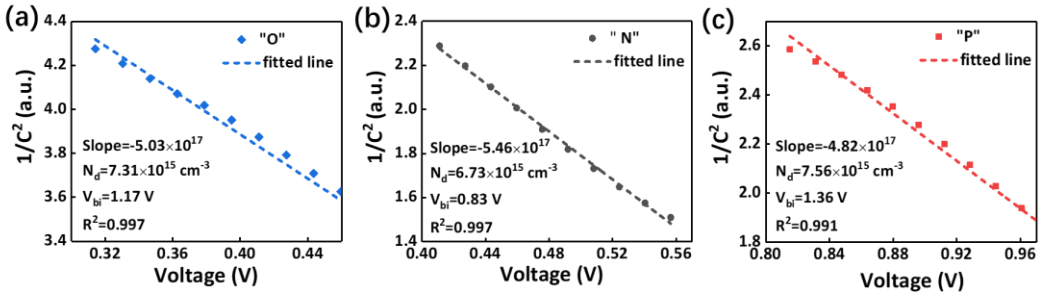

Figure S6. Mott-Schottky characterization fitting results of quasi-2D PVSCs: (a) "O" (no ion accumulation), (b) "N" (unfavorable ion accumulation) and (c) "P" (favorable ion accumulation). As presented by equation S1, the slope of $1/C^2$-V curve states the dopants concentration of absorber layer.

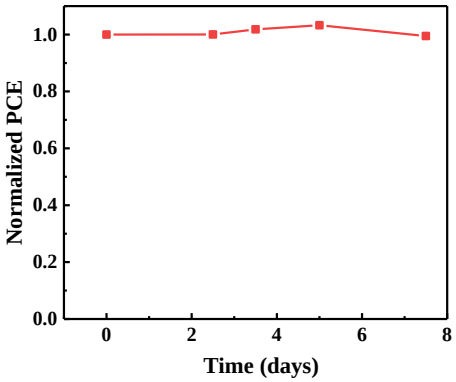

Figure S7. Variation in the PCE of the thermal-light co-treated device over the storage time in N_2 at room temperature in the dark.

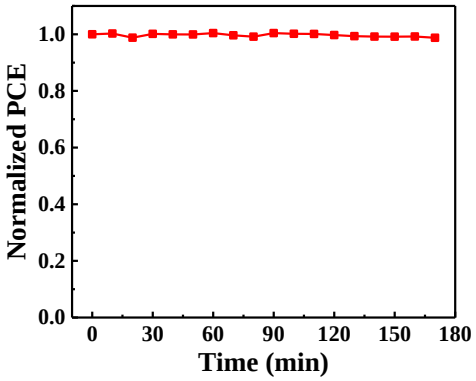

Figure S8. The stability of the devices with "P" under MPP continuous operational condition.

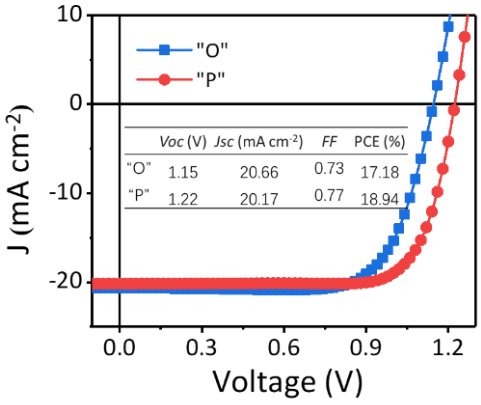

Figure S9. *J-V* curves and corresponding photovoltaic parameters for the (3AMP)$(MA_{0.75}FA_{0.25})_3Pb_4I_{13}$ based devices without and with thermal-light co-treatment.

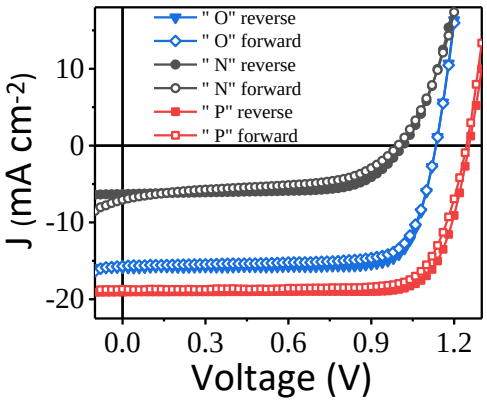

Figure S10. Forward-reverse *J–V* characteristic curves of the quasi-2D PVSCs with different conditions.

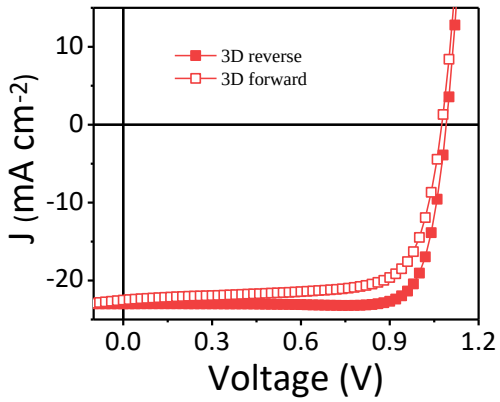

Figure S11. Forward-reverse *J–V* characteristic curves of the 3D PVSC.

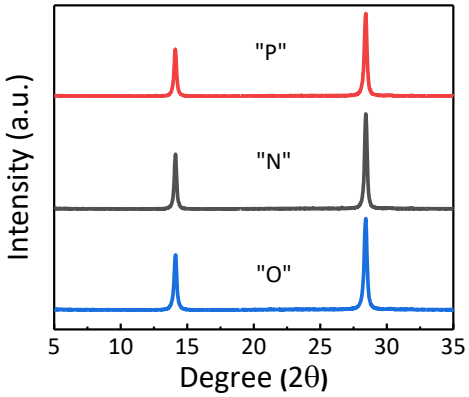

Figure S12. XRD patterns for quasi-2D $GA_{0.2}BA_{1.8}MA_5Pb_6I_{19}$ perovskite with different conditions.

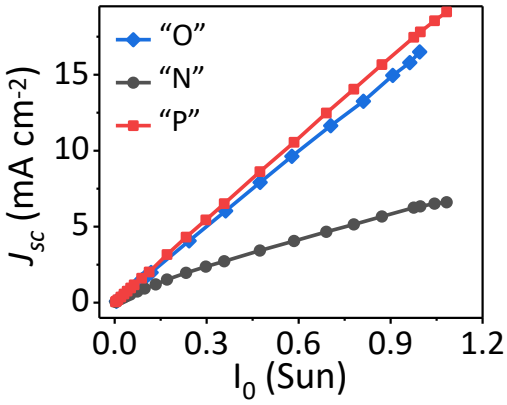

Figure S13. Light intensity (I_0) dependent *Jsc* with different ion accumulations.

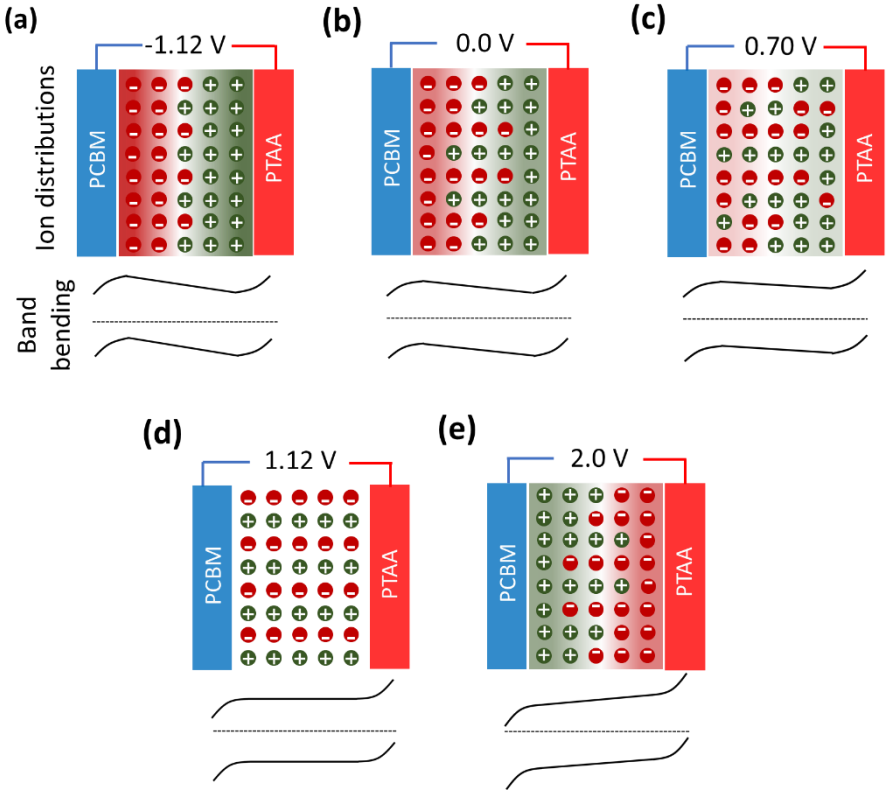

Figure S14. Schematic diagrams of ion distribution (upper) and band bending schematic diagrams (bottom) of quasi-2D $GA_{0.2}BA_{1.8}MA_5Pb_6I_{19}$ PVSCs under different thermal-electrical poling voltages: (a) -1.12 V, (b) 0.0 V, (c) 0.70 V, (d) 1.12 V, (e) 2.0 V.

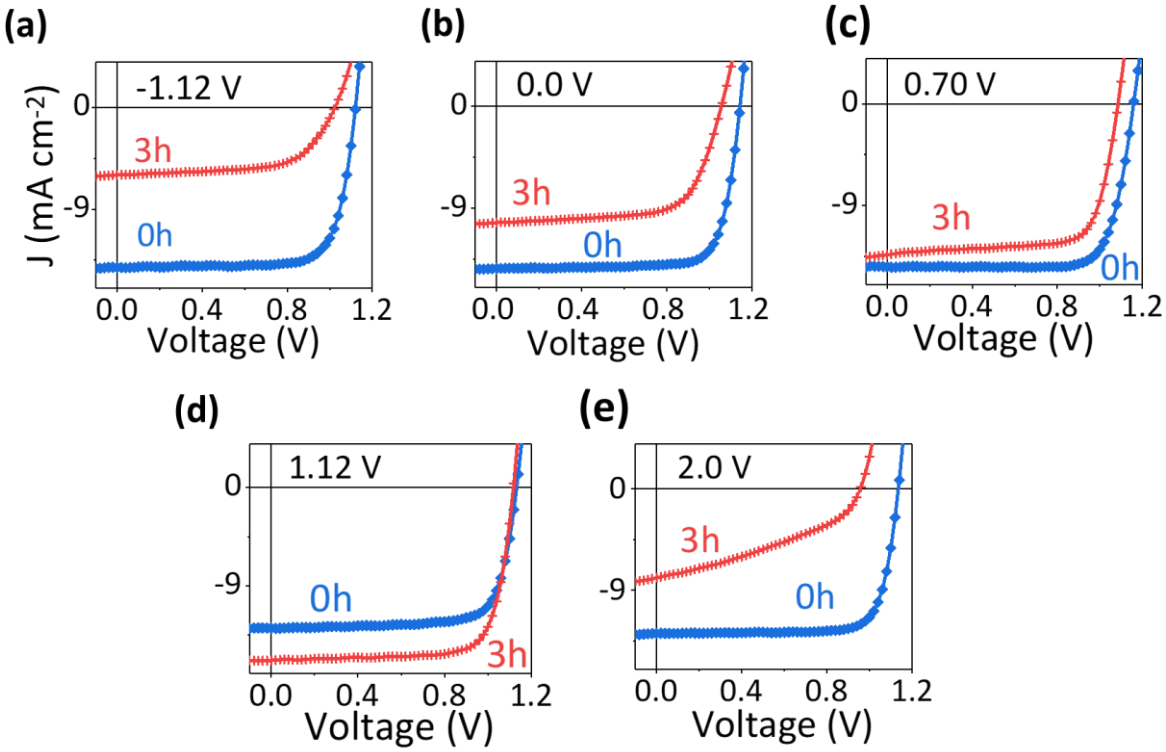

Figure S15. *J-V* curves of quasi-2D $GA_{0.2}BA_{1.8}MA_5Pb_6I_{19}$ PVSCs under different thermal-electrical poling voltages: (a) -1.12 V, (b) 0.0 V, (c) 0.70 V, (d) 1.12 V, (e) 2.0 V.

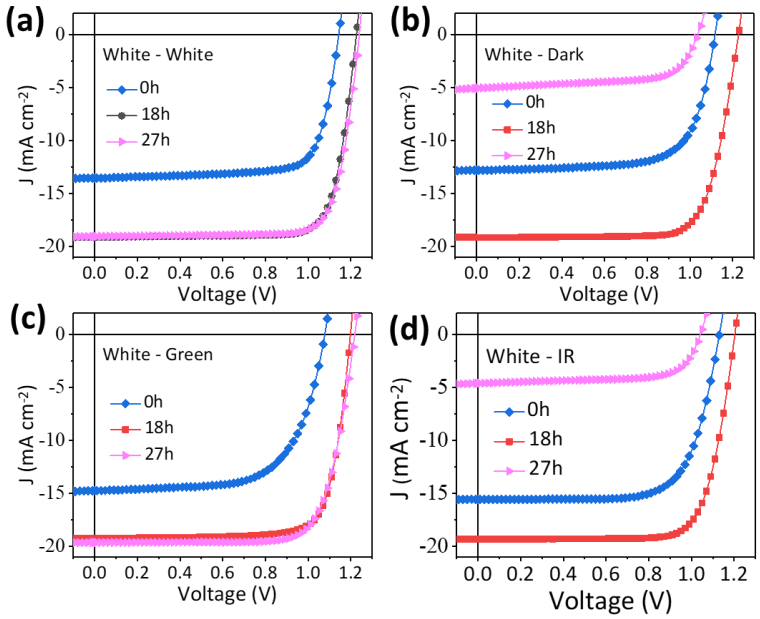

Figure S16. J-V curves for the quasi-2D $GA_{0.2}BA_{1.8}MA_5Pb_6I_{19}$ PVSCs firstly under thermal-light co-treatments, and then further under thermal treatment in dark or under thermal-light activation with different wavelengths.

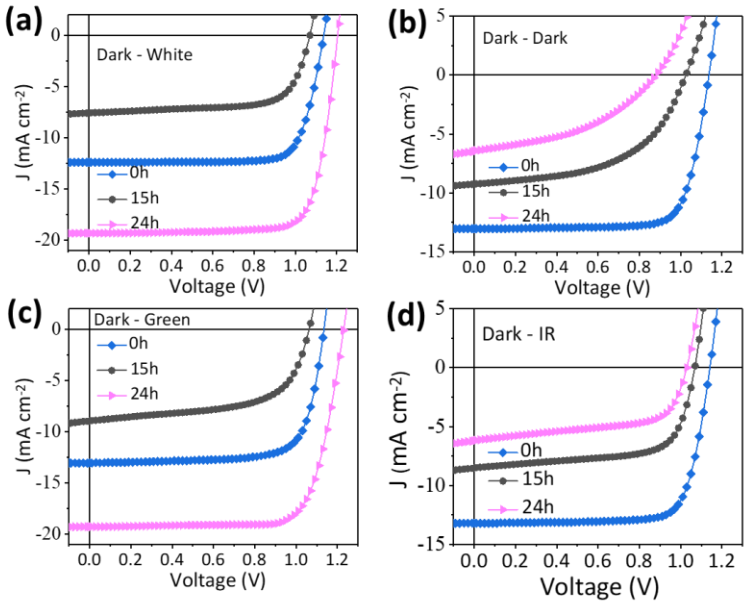

Figure S17. *J-V* curves for the quasi-2D $GA_{0.2}BA_{1.8}MA_5Pb_6I_{19}$ PVSCs firstly under thermal treatment in dark, and then further thermal treatment in dark or thermal-light activation with different wavelengths.

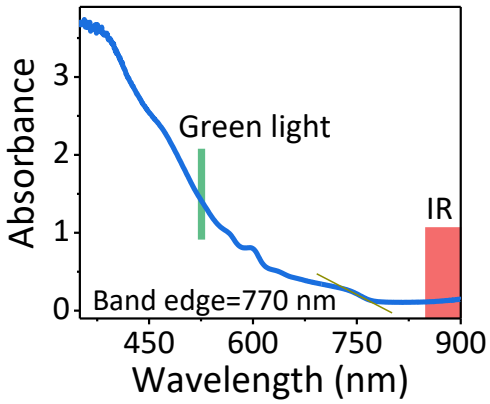

Figure S18. Absorption spectrum of $GA_{0.2}BA_{1.8}MA_5Pb_6I_{19}$ perovskite film.

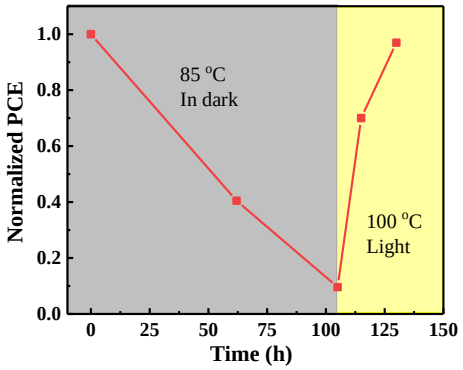

Figure S19. Normalized PCE for the quasi-2D PVSC first stored in the dark at 85 °C for 105h, and then subjected to thermal-light activation (100 °C) for 25h.

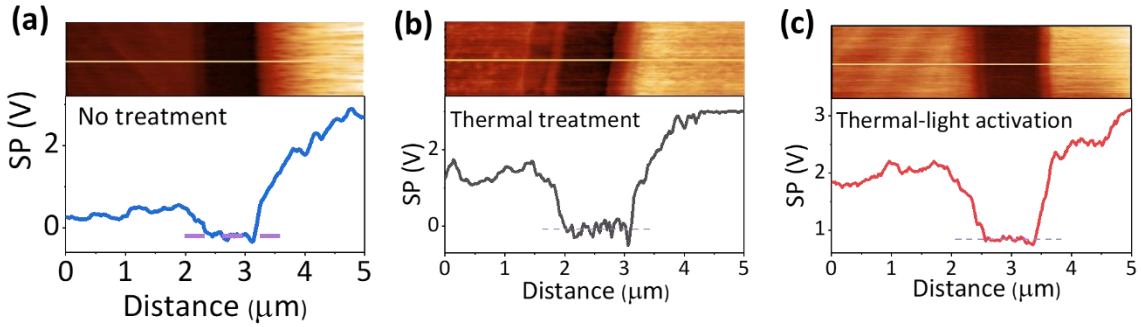

Figure S20. Line profile showing surface potential (SP) distribution taken at the position marked by yellow horizontal line in the cross-sectional SKPM images for 3D $MAPbI_3$ PVSCs, with the device structure of ITO/NiOx/PTAA/$MAPbI_3$/PCBM/BCP/Ag: (a) no treatment, (b) thermal treatment in dark, and (c) thermal-light activation.

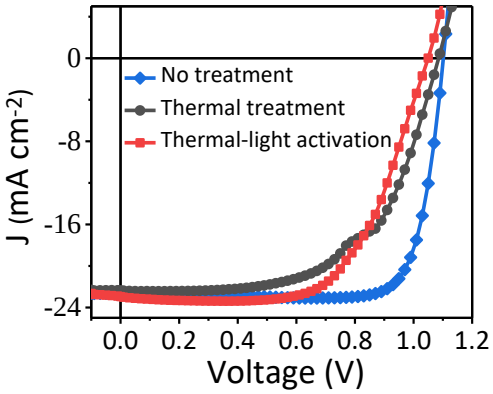

Figure S21. J–V characteristic curves of 3D $MAPbI_3$ PVSCs with different post-treatments (for 16 h).

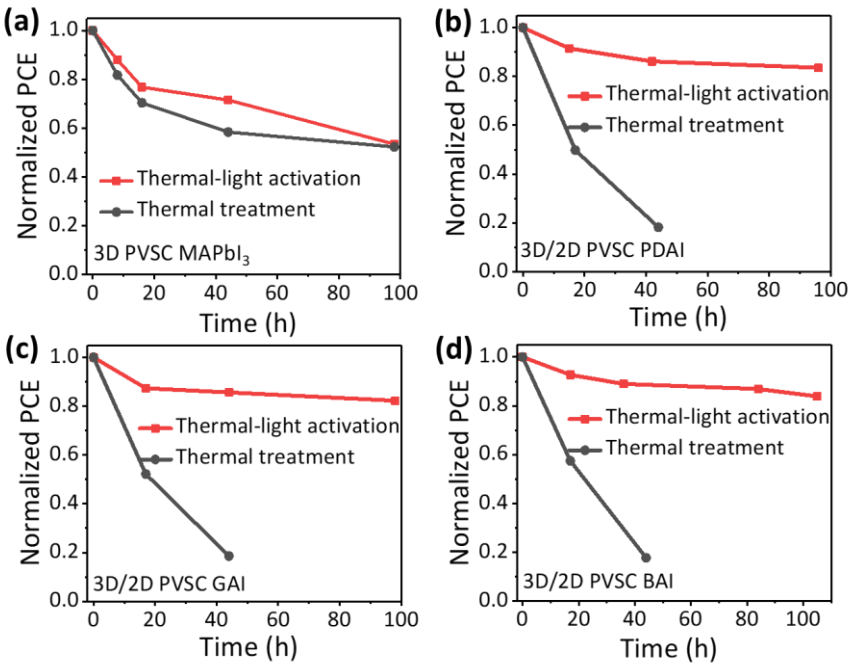

Figure S22. Efficiency variation for the 3D $MAPbI_3$ PVSCs (a) and 3D/2D heterojunction PVSCs with different spacer cations capping on the $MAPbI_3$ perovskite film, (b) PDAI, (c) GAI, (d) BAI with different post-treatments.

Supporting Tables

Table S1. Parameters of ion migration in quasi-2D PVSC and 3D PVSC.

Device	Ions	Activation energy (eV)	Effective diffusion coefficient at 300K ($cm^2 s^{-1}$)	Concentration of mobile ions (cm^{-3})
2D	I^-	0.27	$1.44x10^{-9}$	$2.73 x10^{13}$
3D	I^-	0.17	$1.31x10^{-8}$	$9.17x10^{12}$
3D	MA^+	0.25	$1.95x10^{-10}$	$2.31x10^{13}$

Table S2. Stabilized photocurrent measurements and PCE output at the maximum power point.

Ion accumulation	Bias voltage (V)	*Jph* (mA cm^{-2})	PCE (%)
"N"	0.93	14.79	13.75
"O"	0.81	4.57	3.70
"P"	1.06	17.39	18.43

Table S3. Forward-reverse photovoltaic parameters of the quasi-2D devices with different conditions and 3D PVSC.

		Voc (V)	*Jsc* (mA cm^{-2})	*FF*	PCE (%)	HI(%)
"O"	Reverse	1.13	15.86	0.80	14.38	5.3
	Forward	1.13	15.69	0.77	13.62	
"N"	Reverse	1.01	6.30	0.68	4.34	19.1
	Forward	1.00	7.05	0.50	3.51	
"P"	Reverse	1.25	19.06	0.80	19.05	4.7
	Forward	1.25	18.70	0.78	18.15	
3D	Reverse	1.09	22.99	0.82	20.65	14.5
	Forward	1.08	22.51	0.73	17.65	

Table S4. XRD patterns parameters for quasi-2D $GA_{0.2}BA_{1.8}MA_5Pb_6I_{19}$ perovskite with different conditions.

	Plane	(111)	(202)
"O"	FWHM (°)	0.263	0.272
	Intensity (cps)	1.2×10^4	2.0×10^4
"N"	FWHM (°)	0.227	0.241
	Intensity (cps)	1.2×10^4	2.1×10^4
"P"	FWHM (°)	0.237	0.256
	Intensity (cps)	1.0×10^4	1.8×10^4

Table S5. Summary on device performance variation under different thermal-electrical poling voltages.

Bias (V)		*Voc* (V)	*Jsc* (mA cm^{-2})	*FF*	PCE (%)	Ratio
-1.12 V	B	1.12	14.14	0.76	12.12	0.32
	A	1.02	5.97	0.64	3.88	
0.0 V	B	1.14	14.33	0.78	12.84	0.57
	A	1.06	10.27	0.68	7.34	
0.7 V	B	1.16	14.43	0.78	13.12	0.81
	A	1.09	13.36	0.73	10.59	
1.12 V	B	1.13	12.87	0.76	11.06	1.22
	A	1.12	15.81	0.76	13.46	
2.0 V	B	1.14	12.82	0.79	11.51	0.25
	A	0.96	7.89	0.38	2.84	

Table S6. The variation of PCE for the quasi-2D $GA_{0.2}BA_{1.8}MA_5Pb_6I_{19}$ PVSCs firstly under thermal-light activation, and then further under thermal treatment in dark or under thermal-light activation with different wavelengths.

Devices	Light	Time (h)	*Voc* (V)	*Jsc* (mA cm^{-2})	*FF*	PCE (%)
1	White	0	1.14	13.63	0.76	11.82
		18	1.23	19.13	0.79	18.59
	White	27	1.24	19.05	0.79	18.67
2	White	0	1.12	12.80	0.71	10.09
		18	1.23	19.16	0.76	17.84
	Dark	27	1.05	5.06	0.66	3.45
3	White	0	1.13	14.75	0.65	10.39
		18	1.14	19.26	0.78	18.06
	Green	27	1.14	19.65	0.76	18.20
4	White	0	1.13	15.57	0.71	12.58
		18	1.20	19.33	0.76	17.75
	IR	27	1.04	4.62	0.69	3.34

Table S7. The variation of PCE for the quasi-2D $GA_{0.2}BA_{1.8}MA_5Pb_6I_{19}$ PVSCs firstly thermal treatment in dark, and then further thermal treatment in dark or thermal-light activation with different wavelengths.

Devices	Light	Time (h)	*Voc* (V)	*Jsc* (mA cm^{-2})	*FF*	PCE (%)
1	Dark	0	1.14	12.40	0.79	11.07
		15	1.07	7.58	0.70	5.68
	White	24	1.20	19.33	0.78	18.26
2	Dark	0	1.14	13.10	0.77	11.46
		15	1.03	9.26	0.53	5.03
	Dark	24	0.88	6.46	0.43	2.44
3	Dark	0	1.13	13.06	0.75	11.08
		15	1.06	8.95	0.60	5.73
	Green	24	1.23	19.29	0.76	17.96
4	Dark	0	1.14	13.21	0.77	11.69
		15	1.07	8.52	0.67	6.11
	IR	24	1.03	6.20	0.60	3.86

Table S8. Variation of PCE for the quasi-2D PVSC firstly stored in dark with 85 °C for 105h, and further thermal-light activation (100 °C) for 25h.

Time (h)	*Voc* (V)	*Jsc* (mA cm^{-2})	*FF*	PCE (%)
0	1.21	17.74	0.78	16.73
62	1.00	10.13	0.67	6.77
105	0.85	4.67	0.40	1.60
115	1.14	14.47	0.71	11.71
130	1.20	17.48	0.77	16.22

Table S9. Summary of the photovoltaic parameters of 3D $MAPbI_3$ PVSCs with different post-treatments (for 16 h).

Treatment methods	*Voc* (V)	*Jsc* (mA cm^{-2})	*FF*	PCE (%)
No treatment	1.10	22.65	0.81	20.27
Thermal-treatment	1.09	22.36	0.59	14.27
Thermal-light activation	1.05	22.95	0.63	15.29

References

1 M. H. Futscher, J. M. Lee, L. McGovern, L. A. Muscarella, T. Wang, M. I. Haider, A. Fakharuddin, L. Schmidt-Mende and B. Ehrler, *Materials Horizons*, 2019, **6**, 1497-1503.

2 M. L. Cai, N. Ishida, X. Li, X. D. Yang, T. Noda, Y. Z. Wu, F. X. Xie, H. Naito, D. Fujita and L. Y. Han, *Joule*, 2018, **2**, 296-306.

3 Z. X. Zhao, X. Y. Chen, H. Q. Wu, X. M. Wu and G. Z. Cao, *Adv. Funct. Mater.*, 2016, **26**, 3048-3058.

4 S. W. Boettcher, S. Z. Oener, M. C. Lonergan, Y. Surendranath, S. Ardo, C. Brozek and P. A. Kempler, *ACS Energy Lett.*, 2020, **6**, 261-266.

5 M. Zhang, Q. Chen, R. Xue, Y. Zhan, C. Wang, J. Lai, J. Yang, H. Lin, J. Yao, Y. Li, L. Chen and Y. Li, *Nat. Commun.*, 2019, **10**, 4593.